LAWRENCE
LIVERMORE
NATIONAL
LABORATORY

LLNL-TR-689786

FInal Report: First Principles Modeling of Mechanisms Underlying Scintillator Non-Proportionality

D. Aberg, B. Sadigh, F. Zhou

April 21, 2016

Disclaimer

This work performed under the auspices of the U.S. Department of Energy by Lawrence Livermore National Laboratory under Contract DE-AC52-07NA27344.

FINAL REPORT FOR THE PERIOD 2013-2015

PROJECT TITLE: **First Principles Modeling of Mechanisms Underlying Scintillator Non-Proportionality**

webPROJECT NUMBER: LL13-FY13-083-PD05 LAB/CONTRACTOR: LLNL

B&R CODE: NN2001-06 DATE: Jan 1, 2015

PRINCIPAL INVESTIGATOR:	Daniel Åberg, (925) 423-0896
LLNL PROJECT MANAGER:	Jenni Pruneda, (925) 422-3037
LLNL POINT OF CONTACT:	Steve Payne, (925) 423-0570
HQ PROGRAM MANGER:	Arden Dougan, (202) 586-5118
HQ OFFICE MANAGER:	Dave Beach, (202) 586-0346

Team members: Babak Sadigh, Fei Zhou, and Daniel Åberg

This final report presents work carried out on the project "*First Principles Modeling of Mechanisms Underlying Scintillator Non-Proportionality*" at Lawrence Livermore National Laboratory during 2013-2015. The scope of the work was to further the physical understanding of the microscopic mechanisms behind scintillator non-proportionality that effectively limits the achievable detector resolution. Thereby, crucial quantitative data for these processes as input to large-scale simulation codes has been provided. In particular, this project was divided into three tasks: (i) Quantum mechanical rates of non-radiative quenching, (ii) The thermodynamics of point defects and dopants, and (iii) Formation and migration of self-trapped polarons. In the following, the progress and results of each of these subtasks will be detailed.

Prepared by LLNL under Contract DE-AC52-07NA27344.

Contents

1.0 OBJECTIVE

This work aims to further the physical understanding of the microscopic mechanisms behind scintillator non-proportionality, which limits the achievable detector resolution, and provide crucial quantitative data for these processes as input to large-scale simulation codes. There is a general consensus that the non-linear events take place in the low-energy transport (LET) stage after the initial ionization. The light yield from an initial distribution of excitons and free carriers can be predicted by solving coupled reaction-diffusion equations. Of course, obtaining predictive results critically hinges upon the accuracy of the parameters that enter these respective models. In principle, only a very few of the required model parameters can, at least approximately and indirectly, be fitted from experiments. As a result, a first-principles model of these parameters is *necessary* for independent determinations of their values. Current models lack insight into crucial processes related to energy transfer to the activator, defect trapping, and non-radiative quenching of the excitation density. Therefore, the following three tasks were designed:

Task 1. Quantum Rates: Calculation of excitation density quenching via Auger recombination

Task 2. Activator electronic structure and geometries: Calculation of activator geometries and thermodynamics

Task 3. Formation and migration of self-trapped holes

2.0 TASK I: AUGER RECOMBINATION RATES

In its simplest case, an Auger-type process consists of electrons scattering off each other in an energy- and momentum conserving process. In particular, this can in excited band-gap systems lead to non-radiative recombination of electron-hole pairs. Figure 1 shows a few examples of electron-electron-hole (eeh) and hole-hole-electron (hhe) scattering events and includes unassisted as well as phonon and defect-mediated recombination.

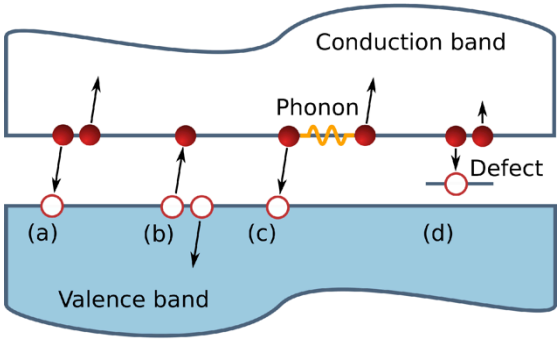

Figure 1: Different Auger recombination processes; (a) direct eeh, (b) direct hhe, (c) phonon-mediated eeh, (d) defect-mediated eeh

The modeling of non-radiative recombination of electron hole-pairs in semi-conductors has received a considerable amount of attention throughout the years. Starting from Fermi's Golden Rule, the pioneering work of Beattie and Landsberg [1] showed that the energy and momentum-conservation rules coupled with thermal occupations lead to exponential dependence in the recombination rates for a simple parabolic two-band system.

With the appearance of modern self-consistent-field theories—such as density functional theory—this was later generalized to more realistic band structures with arbitrary dispersions and more bands [2][3][4]. Consider, for example, the process depicted in Figure 2. The associated transition rate is given by

$$R = 4\pi \sum_{1234} P \left|\langle\psi_1\psi_2|W|\psi_3\psi_4\rangle\right|^2 \delta(\epsilon_1 + \epsilon_2 - \epsilon_3 - \epsilon_4),$$

where P is a thermal occupation factor, W represents the screened Coulomb interaction and the summation runs over a 12-dimensional reciprocal volume. The dimensionality is reduced to nine because of conservation rules. For clarity, the exchange matrix element has been omitted. Despite the advances in describing the underlying electronic structure, calculated rates have been underestimated. Groundbreaking calculations by Kioupakis and co-workers showed that this could be remedied by inclusion of electron-phonon interaction. [7] [8]. This was however only possible after quite severe, but for certain systems very reasonable, approximations [7]. Nevertheless, the agreement with experiment has become quite satisfactory, at least for semiconducting systems.

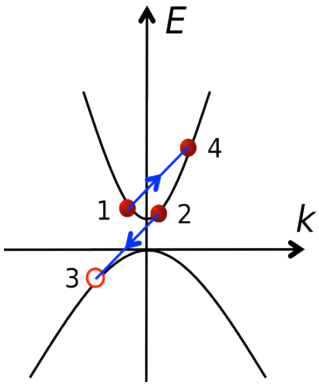

Figure 2: Band model of a direct eeh process during which an electron (1) gets scattered into an excited state (4) and an additional electron (2) recombines and annihilates a hole (3).

2.1 Free carriers in sodium iodide

Until now, there has been no reports on theoretical and very little experimental work regarding Auger recombination (AR) in NaI. Experimental measurements of AR in scintillators are extremely difficult, since each incident gamma-ray photon generates multiple carriers, which can interact through several non-radiative mechanisms that are impossible to discern directly. The analysis of experimental data must then try to relate properties such as the light yield to models that include AR rate parameters. However, different experimental conditions and underlying assumptions used in models can lead to seemingly different AR coefficients spanning many orders of magnitude. Using rate equations for the temporal and spatial evolution of excitation densities, the work in Ref. [9] found an AR coefficient of 1.07×10^{-20} cm^6 s^{-1} when modeling Compton coincidence data from SLYNCI. On the other hand, a much smaller coefficient of 3.2×10^{-29} cm^6 s^{-1} was reported when modeling z-scan experiments using a pulsed laser [10].

Together with researchers at University of Michigan, Ann Arbor, we showed that AR is dominated by the phonon-assisted process at room temperature and is primarily mediated by short-range acoustic and longitudinal optical (LO) phonons. The calculated values for the direct e-e-h AR coefficients are shown in Figure 3.

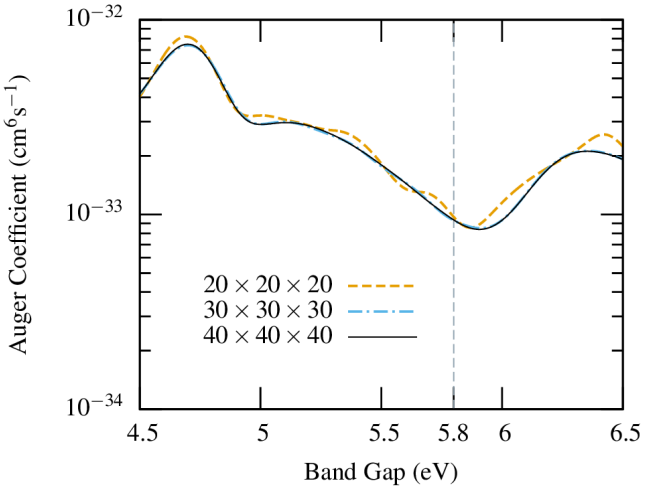

Figure 3: Calculated values for the direct Auger recombination coefficient of NaI as a function of the grid spacing used to sample the BZ and the (rigidly adjusted) band gap of the material.

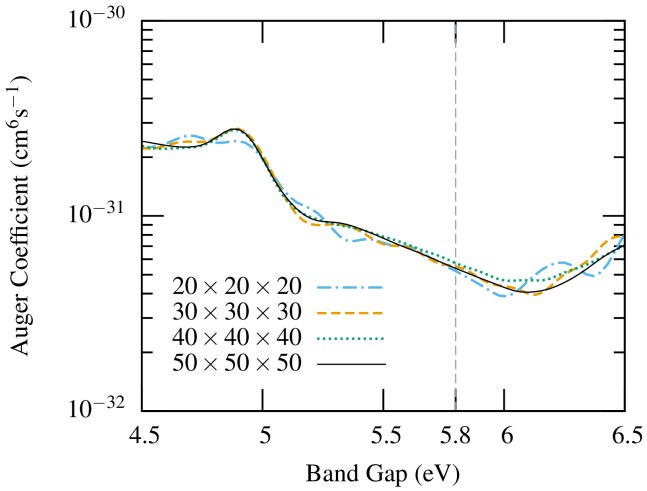

Figure 4: Calculated values for the phonon-assisted direct Auger recombination coefficient of NaI as a function of the grid spacing used to sample the BZ and the (rigidly adjusted) band gap of the material.

To estimate the sensitivity of the calculated coefficients to the band gap value, we adjusted the value of the band gap between 4.5 and 6.5 eV. The calculated value at the experimental band gap is 1.15×10^{-32} cm^6 s^{-1}. Figure 3 shows that a BZ sampling grid of 30x30x30 is sufficient to converge the Auger coefficients. The same figure also shows that the direct Auger coefficient does not depend sensitively on the band gap. For example, if the band gap changes within 60.3 eV from the experimental value (5.8 eV) the direct Auger coefficient changes by at most 50%. The dependence of the direct Auger coefficient on the band gap follows the Arrhenius activation law derived for intraband Auger processes even though direct AR in NaI occurs through interband processes to higher conduction bands.

The phonon-assisted AR coefficients are shown in Figure 4 as a function of the band gap. The value of the phonon-assisted Auger coefficient at the experimental band gap, 5.6×10^{-32} cm^6 s^{-1}, is approximately a factor of 5 larger than the direct one and therefore phonon-assisted processes dominate AR in NaI. We find that AR in NaI is mediated primarily by the acoustic and the LO phonons, while the contribution by the transverse optical (TO) modes is approximately one order of magnitude smaller. Indeed, the dominant contributions occur at wave vectors comparable to the BZ dimensions that correspond to phonon wavelengths comparable to the lattice constant. Therefore, AR in NaI is primarily assisted by short-range phonon scattering.

Comparing with the coefficients fitted to experimental data, we note that our calculated rate is several orders of magnitudes smaller than the value of 1.07×10^{-20} cm^6 s^{-1} obtained by Bizarri *et al.* [9]. We note however that

recently more improved sets of rate equations and boundary conditions have been developed. Comparing to more recent results from fits ($3.2x10^{-29}$ cm^6 s^{-1}) to z-scan experiments, our calculated values are off by a few decades [10]. This illustrates the difficulty in fitting a rate equation model to a very complex set of events and interdependent mechanisms. While one possible cause for the difference between our results and experimental data is thallium doping present in NaI samples that were studied in experiment, we note that Ref. [10] has considered both pristine and Tl-doped CsI with only a small variation (a factor of about 1.5) of the AR coefficients. We therefore expect that the inclusion of dopants does not have a large effect on the AR rate.

Interestingly, for a wide range of materials, Williams et al., noted an empirical band-gap rule. [10] This trend was however not followed by the halide systems under consideration, which instead displayed values that exceeded the expected values by three to four orders of magnitude. The plausible explanation by the authors was the following: (i) the underlying model and assumptions are wrong or insufficient, or (ii) the excitation energy exceeds the band gap of NaI by about 0.3eV (3500K electronic temperature) and might leave the carriers with very high electronic temperatures, or (iii) the Auger recombination might involve self-trapped holes (Vk-centers) with localized hole states in the forbidden gap. We note that our predicted value actually obeys the observed empirical band gap rule. To assess the effect of high electronic temperature on AR coefficients, we performed direct AR calculations for increasing electronic temperatures up to 2500 K

We fitted the data for the experimental band gap of 5.8 eV with an Arrhenius activation law. Using this model, we obtained changes in the direct AR coefficient of at most 50% if the band gap is changed by 0.3 eV as was found in the calculated data. The Arrhenius model finds that the direct AR rate surpasses the calculated low-temperature phonon-assisted rate for electronic temperatures higher than 1360 K. However, even infinite electronic temperature the maximum direct AR coefficient ($2.94x10^{-31}$ cm^6 s^{-1}) is still much smaller than experimental results.

The third possibility of a self-trapped hole to participate in the Auger process is indeed very interesting. Preliminary results indicate that not even introduction of V_K-centers with very localized molecular levels are enough to reach the very large AR coefficients of Williams *et al.*

3.0 TASK 2: DEFECTS AND ACTIVATORS

3.1 Iodine vacancy centers in SrI_2

In 2008, SrI_2:Eu became the focus of intense interest by setting a new record in scintillator performance with arguably the best combined light yield and proportionality achieved to date. Interestingly, the recent top performers so far are always in host crystals describable as multivalent or complex metal halides. According to a model by Li et al.[11], a main reason for the better performance of complex halides over simple alkali halides involves both hot electron transport within the dense ionization track and the concentration and properties of deep electron traps in the host. Together, the diffusion distance, trap concentration, and capture cross-sections determine a linear quenched fraction, which was shown in Ref. [12] to be a controlling factor in both nonproportionality and the total light yield.

Part of the motivation of this work is to gain understanding of electron traps contributing to the size of the linear quenched fraction and furthermore to characterize the properties of some of the expected common lattice defects in SrI_2. As it turns out, SrI_2 is extremely hygroscopic, and until recently it was moderately difficult to grow good crystals. As a result of these complicating experimental factors and the absence of a strong driving interest until the recent need for improved gamma detectors, there is very little known about defects in SrI_2. Thermoluminescence measurements have been performed. However, optical absorption and EPR spectroscopy of native or radiation induced lattice defects in SrI_2 are basically absent. In this light we have undertaken a detailed study of the iodine vacancies (F-centers) in SrI_2.

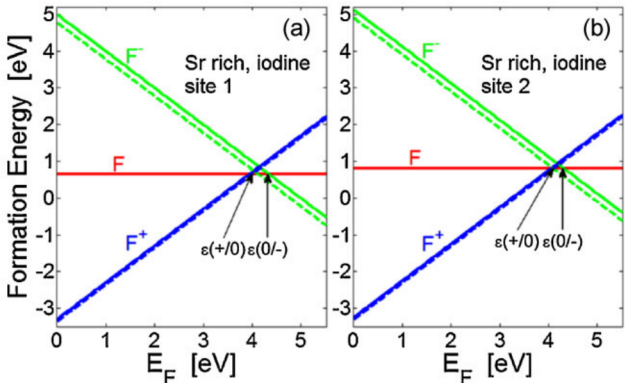

Figure 5: Formation energies of vacancies at iodine sites 1 and 2 under Sr-rich conditions are plotted in (a) and (b).

The formation energies for at the F-center in Sr-rich limit for three different charge states as a function of Fermi energy are shown in Figure 5. Note that there are two distinguishable iodine sites in the crystal – site 1 has four nearest Sr ion neighbors and site 2 has three nearest Sr ion neighbors. The F center at site 1 has ~0.2 eV lower formation energy than at site 2, which indicates that type 1 will be the prevalent one.

We used an interpolation scheme to construct configuration coordinate diagrams for the F and F□ centers based on the first- principles defect energies at lattice configurations along the linearized configuration path from the potential minimum to the ionized equilibrium configuration for each of the defect charge states. Thermal trap depth and optical trap depth are directly obtained from first principles, 1.56 and 1.17 eV for the neutral and negatively charged F-center, respectively. In SrI_2, thermoluminescence is one of the first defect spectroscopies other than luminescence that has been published. Yang et al.(Ref [13]) found 9 thermoluminescence peaks in the temperature range 50–259 K, and none in the range 260–550K. The highest activation energy (thermal depth) in the measured range was 0.431 eV for the 255 K peak. The others were lower than 0.28 eV. None of these are a good match for the calculated F center thermal trap depth in SrI_2. This suggests that the F center and F- center likely function as deep electron traps (effectively quenchers) in SrI_2 after all.

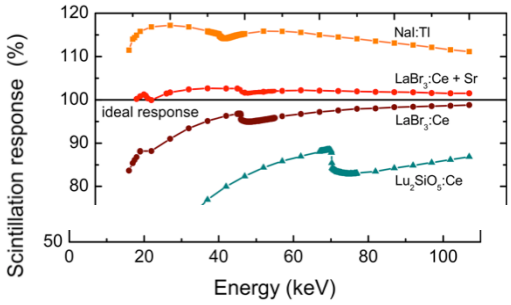

Figure 7: Change in scintillation response for $LaBr_3$:Ce when co-doped with Sr. Note the increased linearity.

Furthermore, construction of the configuration coordinate diagram permits determination of the effective ground and ionized state force constants from fitting the first-principles potential curves. This allows calculating the ground-state and ionized-state defect vibrational wave functions for prediction of optical lineshapes. Departing from first principles methods, but using the results noted above to remove large uncertainties surrounding appropriate e and m* parameters in the simple hydrogenic model of F center optical transitions, we were able to use that model to make interpolations of excited state energies based on the 2.31eV energy interval from ground to ionized state of the defect rather than the 13.6 eV Rydberg basis of the full hydrogenic model. In this way the uncertainties in excited state energies of the F center become of a tolerable size to make meaningful comparisons and predictions with experiments. For example, the vibrationally broadened 1s→ 2p optical absorption of the F band in SrI_2 was predicted as a simpler alternative to the GW and BSE predictions of F^+ and F bands as has been used in MgO

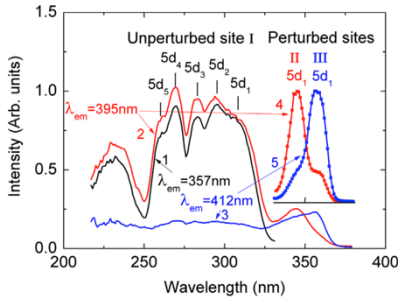

Figure 7: Photoluminescence excitation spectra clearly demonstrating at least three different Ce-sites in Sr-doped $LaBr_3$:Ce.

3.2 Aliovalent co-doping of $LaBr_3$

One of the best materials for detector performance is Ce-doped $LaBr_3$[14]. It yields an energy resolution of 2.7% at a photon energy of 662 keV in combination with an extremely fast scintillation pulse. $LaBr_3$ has been very well characterized both experimentally [15][16] and theoretically [17][18][19][20] The prospect of improving energy

resolution by co-doping $LaBr_3$:Ce with Sr or Ba was first noted experimentally by Yang and coworkers [21]. Later Alekhin *et al.* revisited this aspect, and by co-doping with Ca and Sr, achieved a record-breaking improvement of energy resolution down to 2.0% at 662 keV (see Figure 7). A more comprehensive investigation that included both the alkaline as well as earth-alkaline series revealed that better performance is only achievable when using the heavier elements earth-alkalines (Sr, Ca, Ba) [23]. The experimental investigations also revealed three distinct optical signatures associated with Ce, which have been interpreted as evidence for the presence of three different Ce environments in the co-doped material (see Figure 7).[24] In contrast, only one such feature can be identified in $LaBr_3$:Ce. Several possible mechanisms were tentatively proposed to rationalize these observations: (a) reduction of the nonradiative recombination rate, (b) an increase of the so-called escape rate of the carriers from the quenching region, or (c) an increase in the trapping rate of Ce^{3+}.

To determine the mechanism behind the improvement, we conducted extensive point-defect calculations for all relevant intrinsic and dopant configurations [25][26]. We identified the bromine vacancies V_{Br} as the energetically most favorable donor-type defect under both La and Br-rich conditions. Additionally, we found that both strontium and cerium are substitutes on lanthanum sites, with the resulting $Sr_{La}(-1)$ defect acting as a shallow acceptor with a vanishingly small lattice distortion while the neutral Ce_{La} defect causes a slight outward relaxation of the neighboring Br atoms. Charge compensation of Sr_{La} is accomplished via introduction of Br vacancies. We show that for the experimental Sr concentration of 200 ppm, the concentration of Br vacancies increases by several orders of magnitude, as shown in the left panel of Figure 8. If these *induced* Br vacancies were left to their own devices, electrons trapped in their deep trap levels would not be able to escape and hence would cause a reduction in the scintillation light yield.

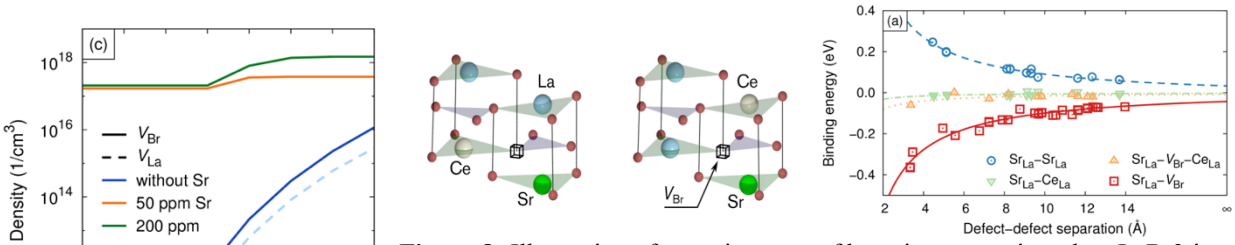

Figure 8: Illustration of steep increase of bromine vacancies when LaBr3 is doped with Sr (Left). Example of different defect complex geometries giving rise to the observed spectra (Middle). Binding energies of various dopant/defect complexes (Right). The red curve in the right figure clearly illustrates the strong binding between the Sr and Br vacancy. Binding is beneficial since the complexes are associated with shallower trap levels.

However, the opposite charge states of V_{Br} and Sr_{La} cause a mutual attraction (right panel of Figure 8), resulting in defect complexes of the type illustrated in the middle panel of Figure 8. As a result, the deep level associated with the vacancies moves closer to the CBM and becomes a much shallower level. Also, the large concentration of Ce (5%) implies that the each defect complex will have Ce in its vicinity. As a result, the experimentally observed different Ce sites emerge, and their measured Stokes shifts agree very well with those predicted from our calculations. For a Ce-only doped system, the rate-limiting step in the assumed sequential hole and electron capture by cerium allows for a substantial quenching of electron-hole pairs by Auger recombination. In a system co-doped with Sr, however, electrons temporarily trap on the shallow complex trap levels and thus reduce the available density subject to Auger recombination. This allows for a larger trapping of hole carriers by the Ce 4f level. Coulombic attraction then serves as a driving force for transferring the electron from the complex to the activator. This suggests that non-linear quenching is reduced at the cost of longer decay-times. In fact, two of the three cerium sites discussed in Ref. [24] are associated with very long decay times—ranging from 60 to 2500 ns—while still accounting for 20-45 % of the total light output. These findings form the core of the framework that will be used to evaluate candidate co-dopants to guide the Venture's search for high-resolution scintillators.

4.0 TASK 3: SELF-TRAPPED HOLES

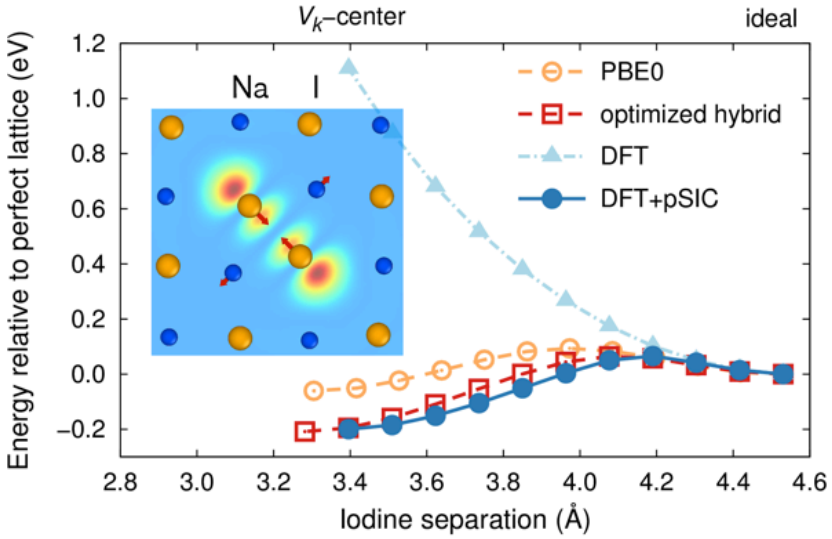

Figure 9: Energy as a function of iodine dimer bond length for the hole polaron in NaI, clearly showing that DFT fails to predict stable polarons while hybrid functionals and the new pSIC method do. The inset shows the atomic configuration the polaron. We will use our new pSIC methodology to accurately predict formation of self-trapped excitons in scintillators.

In materials with at least partially ionic bonding character, most notably halides and oxides, charge excitations can couple to lattice modes, leading to the formation of polarons. In the limit where the coupling between charge excitations and phonons is strong, one obtains so-called small or Holstein polarons, which are characterized by very large but localized lattice distortions. Their motion can be considered classical and typically exhibits an exponential temperature dependence. As a result the presence of polarons usually implies low mobilities, which are detrimental for many applications. In halide scintillators, a pair of nearest-neighbor halogen ions can dimerize and trap a hole, leading to a structure of the type shown in the inset of Figure 9 (known as a V_K-center). Density functional theory (DFT) is a computationally efficient parameter-free methodology for calculating chemical and electronic properties of materials from first principles. While it has been widely successful for many applications, DFT fails qualitatively to describe polaron formation in insulators [27] (see light-blue curve in Figure 9). Hybrid-DFT methods that combine DFT with exact exchange (EX) or screened exchange (SX) provide a framework to predict polaron formation in insulators (see Figure 9). Today, hybrid functionals constitute the state of the art for predicting structural and electronic properties of polarons and STEs in insulators. These methods are, however, computationally very expensive, which has limited their applicability to mainly static properties of polarons, and kinetic studies of carrier self-trapping and polaron transport have remained daunting. As another disadvantage, hybrid-DFT methods contain adjustable parameters that need to be fitted to some known material property. Other methods that mimic hybrid functionals within localized atomic spheres have emerged, but they lack the generality to cope with molecular polarons [28][29][30].

To address this issue, we have devised a ***parameter-free, accurate, and fast*** algorithm to replace the costly hybrid functionals. This method does not suffer from the limitations of atomic spheres. It builds on the key realization that DFT's failure is due to a self-interaction (SI) error of the localized polaron and that DFT provides a physically sound description of the neutral (but not the charged) state—see Figure 10. In practice, the new methodology, which is termed the *polaron self-interaction correction* (pSIC) method, modifies the DFT functional by writing the total energy of the charged system as

$$E_{\mathrm{pSIC}}(q = \pm 1) = E_{\mathrm{DFT}}(q = 0) \pm \epsilon_{\mathrm{polaron}}$$

This amount to adding/subtracting—depending upon the type of polaron (hole/electron)—the single particle energy level associated with the polaronic state. The central panel of Figure 10 illustrates the effect of self-interaction (SI)

in DFT on its description of polaron self-trapping in NaI. It shows the DFT total energy for both the ideal lattice (dotted red line) and the V_K-center configuration (solid blue line) represented by a 216-atom supercell as a function of fractional hole charge. Whereas the variation is almost perfectly linear for the ideal lattice, in the case of the V_K-center configuration, a pronounced convexity is apparent. This is the hallmark of SI. The SI can be corrected by removing the curvature, as illustrated by the dashed green line. This approach to removing the convexity by extrapolating the initial slope is justified by the observation that for the V_K-center configuration in NaI in the neutral charge state, the DFT quasi-particle (QP) energies—apart from a scissors shift—are in good agreement with optimized hybrid-exchange functionals and many-body theories, such as *GW* (see the left panel of Figure 10). In contrast, the right panel of Figure 10 shows that for the charged system, the DFT QP spectrum differs qualitatively from higher-level calculations due to the presence of SI. The resulting functional produces stable polarons in agreement with the best hybrid functionals (see dark-blue curve in Figure 9).

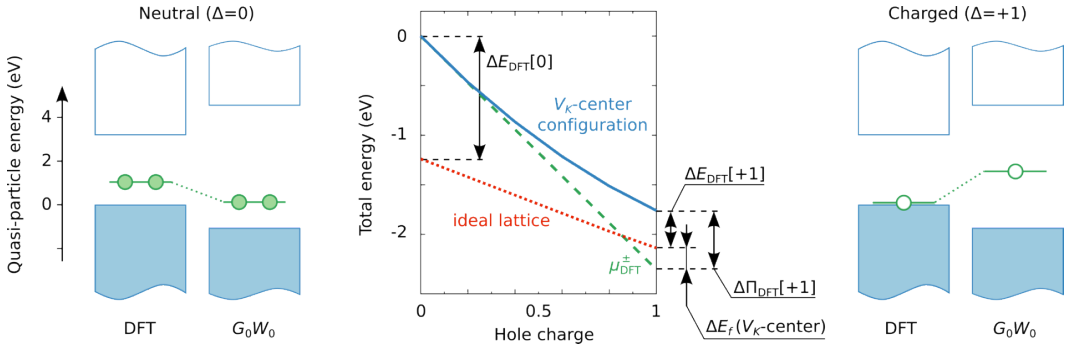

Figure 10: Left/right panel: Quasi-particle energy levels in DFT and a higher level theory in the neutral/charged state. Middle panel: Total energy of the system as a function of the removed charge. The middle panel shows the DFT and pSIC energies for the VK-center configuration (blue and green curves) as well as for the ideal lattice where pSIC is identical to DFT (red curve), all of which illustrates the fact that the failure of DFT to predict stable polarons lies in the curvature of the total energy with respect to removed charge.

Our algorithm has taken the field into a new paradigm where we can now routinely study formation of polarons (both holes and electrons) in arbitrary materials without having to resort to costly and parameter-dependent hybrid calculations. In the following sections, we will discuss some relevant calculations and predictions of the pSIC approach:

4.1 Alkali Halides

4.1.1 Formation energies

The pSIC total energy functional can be written as

$$E_{\text{pSIC-DFT}} = E_{\text{DFT}} + \mu_{\text{DFT}}$$

Here E_{DFT} represents the DFT total energy of a specific configuration (leftmost point of red/blue curves in Figure 10) and μ_{DFT} represents the electron chemical potential of that system (derivative of red/blue curve at the same point). Thus, pSIC, when based on DFT, produces stable hole polarons in NaI. As already mentioned, the computational cost of a DFT-pSIC is magnitudes lower than a hybrid calculation, but there is still a reason to pause for a study the application of pSIC on top of hybrid functionals. To this end, we study polaron formation energies as a function of fractional exact exchange, α, used in a hybrid functional. α ranges from 0 (pure DFT) to 1 (pure Hartree-Fock). At some intermediate value α_{OPT} the band gap matches a DFT-GW calculation, and at this point the self-interaction should be minimal.

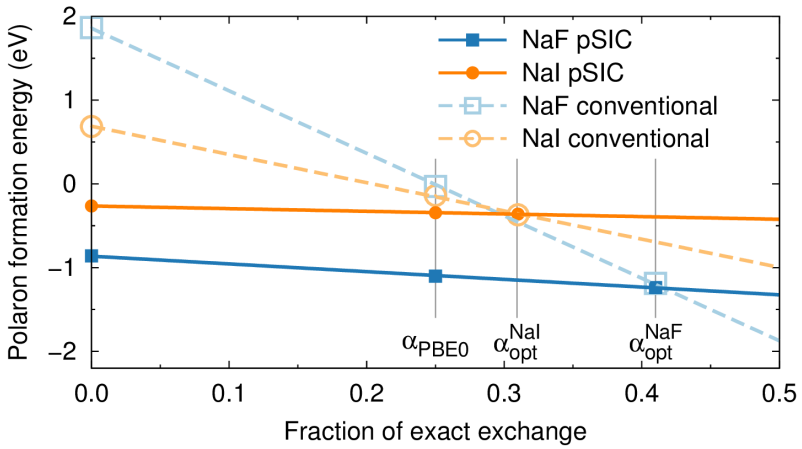

Figure 11: Variation of the calculated polaron for- mation energies of NaI and NaF with the mixing parameter of the hybrid XC functional.

Figure 11 shows polaron energies as a function of the hybrid mixing parameter, α, for two alkali halide compounds NaI and NaF, calculated using the conventional and the pSIC methods. Note that the polaron energies vary significantly with mixing, when calculated using the conventional energy functional whereas they depend very weakly on α, when calculated using the pSIC functional. The insensitivity of the pSIC- pSIC-hyb hybrid functional to parametrization is the main advantage of the pSIC method. It allows for accurate predictions of polaron energies with α set to zero, i.e., pSIC-DFT. In this way the computational cost of the calculations can be reduced significantly compared to hybrid functionals, and brought to be on par with simple DFT calculations with a minor impact on accuracy.

In the following, we further evaluate the accuracy of the pSIC-PBE method by an extensive study of its predictions for the V_K centers in alkali halides. These compounds constitute a diverse class of wide-gap insulators with band gaps ranging from 5 to 14 eV and lattice constants from 4.0 to 7.3 Å. We compare the results of pSIC-PBE calculations with conventional hybrid-XC calculations using two distinct parametrizations: (i) the PBE0 functional [4], which uses a fraction of 0.25 of exact exchange (EX) , and (ii) a set of optimized hybrid functionals, which have been parametrized to reproduce PBE+GW calculations. For these compounds, the fraction of EX used in the optimized hybrid calculations vary from 0.25 in LiI to 0.41 in NaF. The results of pSIC-PBE and hybrid calculations are compiled in Figure 12, which shows (a) the halogen-halogen separation at the core of the V_K-center, and (b) the V_K-center binding energies. With regards to the halogen dimer separations, it is evident that the pSIC-PBE method yields excellent agreement with hybrid calculations with a typical deviation of less than 0.15 Å.
Figure 12b shows that the polaron binding energies calculated within pSIC-PBE agree well with the results from optimized hybrid calculations. Overall, pSIC-PBE yields polaron binding energies that are 10% to 20% smaller than those from optimized hybrids. On the other hand, for most materials considered here, especially those with larger band gaps, the PBE0 functional, in the conventional mode of calculation, predicts V_K-center binding energies that are much smaller than either pSIC-PBE or optimized hybrid calculations.

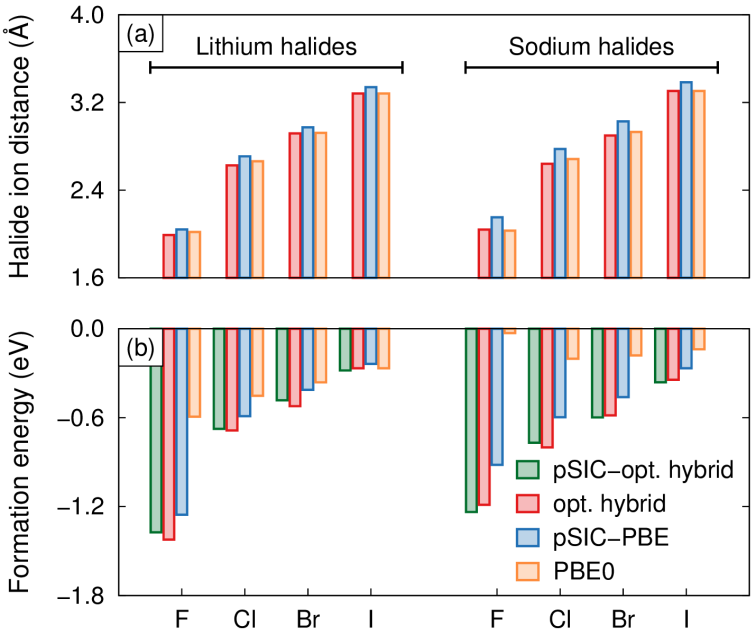

Figure 12: Comparison of (a) halogen-halogen sepa- ration at the core of the V_K -center and (b) V_K-center binding energies between pSIC-PBE and hybrid-DFT calculations.

4.1.2 V_K-center migration in NaI

Thanks to its computational efficiency, the pSIC-DFT method provides an unprecedented potential for studying polaron dynamics. To demonstrate this aspect, we also bench- mark calculated polaron migration barriers with measured diffusivities in NaI. By symmetry, the migration of an I_2^- dimer to a nearest-neighbor site in the rocksalt lattice can involve rotations through 60, 90, 120, or 180 degrees, the last one corresponding to a pure translation. The polaron diffusivity in alkali halides can be accurately measured in laser pump-probe experiments [32]. To this end, VK centers are created and aligned along a particular direction ("polarized") using a pump laser. Subsequently, the gradual loss of polarization over time is followed using a probe laser, from which rotational barriers can be inferred. Experiments cannot distinguish between 60 and 120 degree rotations and are insensitive to migration via translation. In NaI at 50 K, one observes almost exclusively 60/120 degree rotations [32], indicative of the fact that their activation barriers are noticeably smaller than for 90 degree rotations. It was similarly shown that 60/120 degree rotations dominate in RbI. Table 1 shows activation barriers calculated within the pSIC-PBE and optimized hybrid approaches using the climbing image nudged elastic band method. Both methods agree very well with each other and with experimental data.

Rotation angle (degrees)	Optimized hybrid	pSIC-PBE	Experiment
60	0.23	0.20	0.2
90	0.28	0.24	> 60 degrees
120	0.23	0.20	0.2
180	0.22	0.19	-

Table 1: Activation barriers for V_K -center migration in NaI in units of eV.

4.2 Electron polaron in Cs_2LiYCl_6

We also demonstrate the accuracy of the pSIC method for electron polarons. For this purpose, we consider Cs_2LiYCl_6 (CLYC), which is one of the most thoroughly investigated compounds in the elpasolite family due to its potential as a neutron detector. Electron polarons have been found in this system both experimentally [33] and theoretically [34] using PBE0 calculations. Its crystal structure (double-perovskite) has cubic symmetry with ten atoms in the primitive cell. The calculated band gap within PBE0 is 7.1 eV, in close agreement with experiment (7.5 eV). Hence PBE0 and optimized hybrid yield nearly identical results for this compound. By comparison, DFT-PBE yields a much smaller band gap of 5.0 eV. We find in accord with Ref. [34] that the electron polaron localizes on a Y site and the polaron level has strong *d* character as shown in Figure 13. Both pSIC-PBE and PBE0 predict a stretching of Y-Cl bonds by about 0.1 Å. The binding energy of the electron polaron is 0.25 eV (0.32 eV) according to pSIC-PBE (PBE0). The PBE0 value for the polaron binding energy includes a significant contribution from image charge corrections of about 0.1 eV due to the small size of the supercells (80 atoms) that was computationally affordable at this time. In fact, performing pSIC-PBE0 calculation of the polaron energy in the ionic configuration obtained from the conventional PBE0 approach, yields a polaron binding energy of about 0.28 eV, in very good agreement with the pSIC-PBE result. This demonstrates that pSIC is also capable of predicting electron polaron geometries and binding energies in close agreement with hybrid calculations.

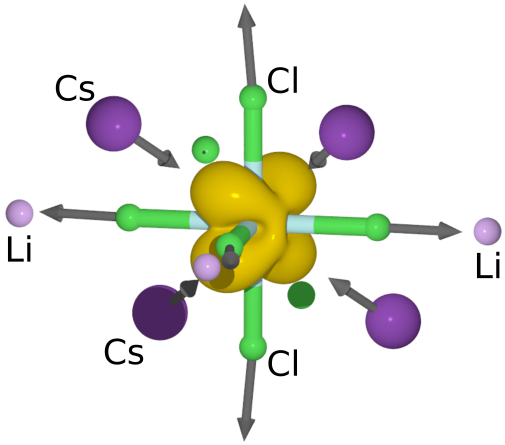

Figure 13: Illustration of the electron polaron in CLYC as obtained from pSIC calculations. The arrows indicate the relaxation pattern. The yellow isosurface is centered at an yttrium atom.

4.3 Hole polaron database

The pSIC methodology has been further exercised for a large number of scintillator materials. In fact, we have now studied hole-polaron formation on all rare-earth activated materials (that we could find crystallographic data for) from the LBNL webpage http://scintillator.lbl.gov/. This amounted to roughly a hundred different compounds and thus constitutes an unprecedented wealth of data on polarons in scintillator materials. The analysis is still underway, and hitherto we have discovered very interesting trends. Firstly, we note that for all halide material, we find the same type of hole polarons; the V_K-center. As expected, the ion separation of the halide-dimer is more or less constant for a given type of halides, see Figure 14.

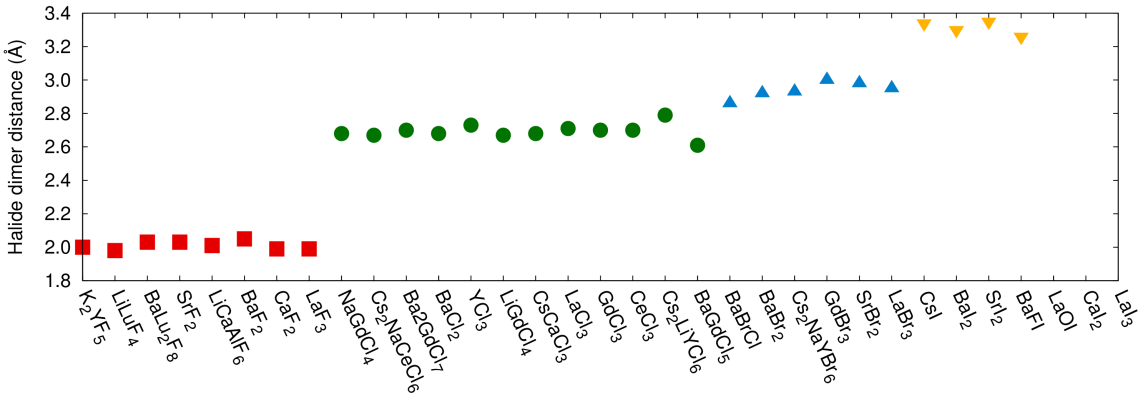

Figure 14: V_K-center bond-length for range of halide materials (a subset)

Furthermore, we observe an approximate linear scaling of the polaron formation energy to the host band gap, see left panel in Figure 15. A similar effect, although more pronounced was earlier found by us for the alkali halides. Thus, more strongly bound polarons are expected in wide-gap materials. We emphasize that the formation/binding energy need to be proportional to any migration barriers. This will be amply demonstrated in the case of SrI_2 in the next section. Here, we are faced a material with strong binding but small barriers.

The database also includes oxide materials. These display, in general, smaller polaron binding energies than the halide systems and at the same time more delocalized polarons – in the sense of atomic displacements (see right panel in Figure 15). Contrary to the V_K-centers, the hole polarons in oxides are typically centered on a single oxygen p-state, but are associated with a long-ranged displacement field with smaller amplitudes. In fact, the displacement field is very reminiscent of a decaying phonon-displacement.

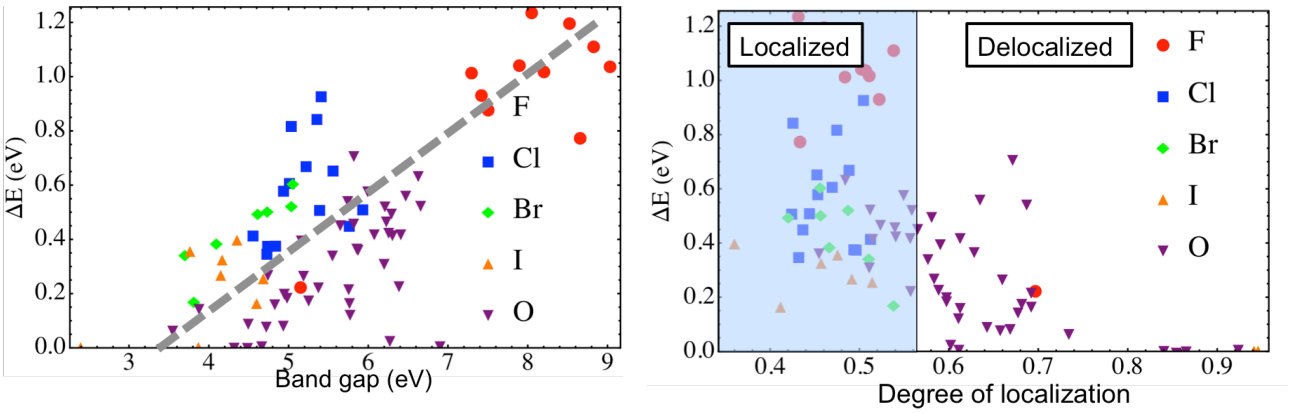

Figure 15: (Left) Polaron formation energy as a function of band gap. Note the linear trend. (Right) Polaron formation energy as a function of degree of localization. Oxides typically have smaller formation energies and tends to be more delocalized.

4.4 Complete mapping of polarons in SrI_2

SrI_2 is contained in the database discussed in the previous section, we already had clues to the complex energy landscape; Firstly, hole polarons in this material are the 'standard' V_K-centers, but has larger binding energies than NaI. However, polaron formation is usually expected to limit carrier mobilities and has been associated with poor scintillator light-yield proportionality and resolution. SrI_2, however, is a very bright scintillator with excellent, record breaking, proportionality. To shed more light on this question the pSIC methodology was used to completely map out the polaronic energy landscape of SrI_2. A random search is like the one employed in the database is however not suitable to identify all possible dimer pairs in a system as complex as SrI_2. Hence a more systematic approach has to be employed. To this end, we considered all symmetrically distinct first-nearest neighbor iodine pairs between two I sites A and B in the ideal structure. To study the polaron migration between dimers A—B → A—C, a systematic exploration of symmetrically distinct iodine triplets A—B—C was performed where I_A—I_B and I_A—I_C are stable dimers. Here, two pairs (triplets) are considered equivalent if there exists a space group operation that maps A—B to A'—B' (A—B—C to A'—B'—C').

The unit cell of SrI_2 [Figure 16 (left)] contains 24 atoms with one Sr and two I sub-lattices, each occupying an 8c Wyckoff site with three degrees of freedom. In this structure, there are 12 symmetrically distinct I—I pairs that are separated by 3.9—5.0 Å, while the second iodine coordination shell is more than 5.7 Å apart. Nine of the possible first-nearest neighbor I—I pairs remain stable after pSIC relaxation, all resulting in a dimer bond-lengths of approximately 3.3 Å [Figure 16 (right)], in accordance with our results for V_K centers in NaI and. The three remaining I--I pairs are unstable with respect to relaxation into one of the nine stable ones.

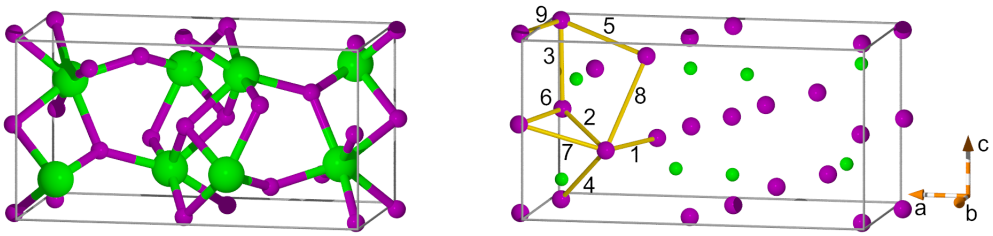

Figure 16: Crystal structure of SrI_2 and hole polaron configurations. (Left) Perspective view of the primitive unit cell; (Right) all stable I—I self-trapped polarons numbered 1 through 9, with only one representative dimer shown per type. Green and lila spheres represent Sr and I ions, respectively.

The formation energies obtained at the pSIC level range from -0.34 eV (configuration **1**) to -0.17 eV (configuration **9**) [Figure 17]. The same figure also illustrates that the formation energies obtained using the pSIC method compare very favorably with the results from the computationally more demanding hybrid PBE0 calculations.

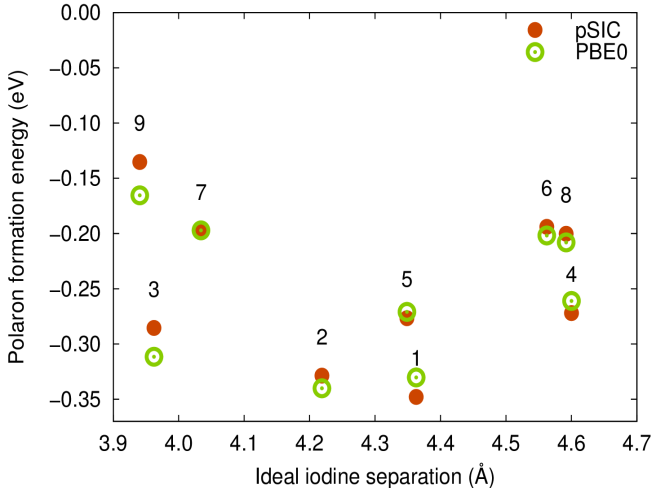

Figure 17: Polaron formation energy vs the initial (ideal) I—I Idimer separation distance from pSIC (filled circles) and PBE0 (squares) calculations obtained using

There exist 66 symmetrically distinct A—B → A—C paths that share one I ion and thus *directly* connect two dimer configurations. Four paths bridge between symmetry-equivalent dimers, such as **1→1'** and **3→3'** [Figure 18 (c-d)]. Most of the transition barriers fall between 0.1 and 0.4 eV with a few paths exhibiting very high barriers of more than 0.6 eV. The three most stable dimers (**1**—**3**) are connected by network with particular low barriers [Figure 18 (b)].

The most stable configurations (**1**) are directly connected via a zig-zag path along the *c*-axis with a barrier height of 0.12 eV. While already this result suggests that polaron diffusion in SrI_2 is much faster than in e.g., sodium iodide where the lowest migration barrier is 0.19 eV, the availability of additional pathways further separates these materials. Specifically, in thermal equilibrium at 300 K the population of type **3** polarons as given by the Boltzmann factor is approximately 5 %. Polarons of this type are accessible from configuration **1** via **2** with an effective barrier of 0.14 eV. They are furthermore connected with each other via a path parallel to the *a*-axis with a barrier of only 0.03 eV, which enables practically barrier free diffusion at room temperature. The exciting ramifications of these low barriers will be examined in the coming lifecycle. We emphasize that these results would not have been possible without the pSIC technique developed within this project. We envision that this fast, yet accurate, method will find many important applications in the future, not only within scintillator physics, but in all systems for which polaron transport is important such as batteries and solid ion conductors.

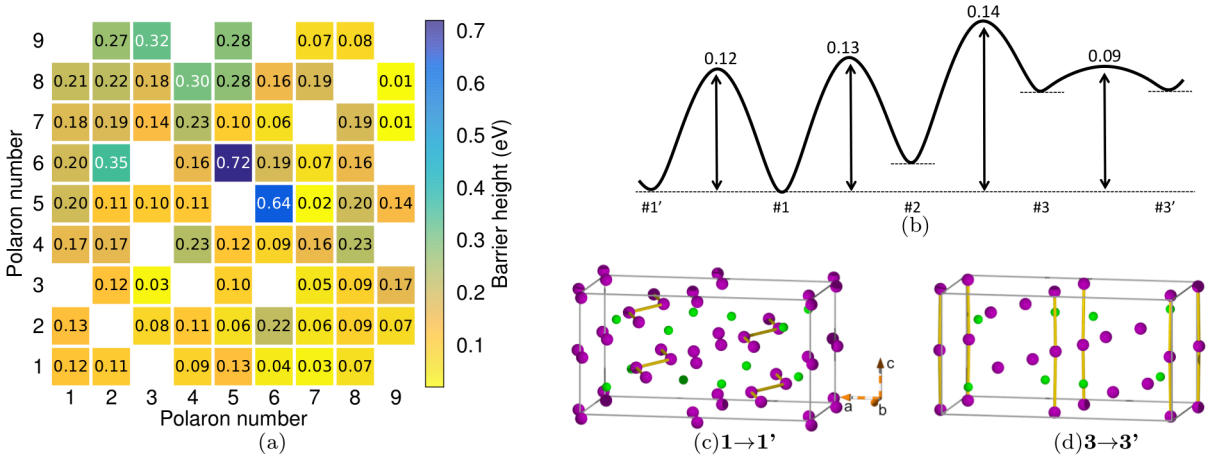

Figure 18: Adiabatic potential energy landscape for polaron migration. (a) Matrix of migration barriers (in eV) separating different dimer configurations. Empty cells in the matrix indicate dimer combinations that do not share an iodine ion and hence are not directly connected. (b) Energy landscape and (c,d) atomic scale representation of efficient (low energy) polaron migration pathways.

5.0 REFERENCES

[1] R. Beattie and P. T. Landsberg, "Auger Effect in Semiconductors," *Proc. R. Soc. Lond.* **249**, 16 (1959);

[2] D. B. Laks, et al., "Accurate interband-Auger recombination in silicon," Phys. Rev. B **42**, 5176 (1990);

[3] S. Picozzi, *et al.*, "Accurate First-Principles Detailed-Balance Determination of Auger Recombination and Impact Ionization Rates in Semiconductors," *Phys. Rev. Lett.* **89**, 197601 (2002);

[4] K. T. Delaney, *et al.,* "Auger recombination rates in nitrides from first principles," *Appl. Phys. Lett.* **94**, 191109 (2009);

[5] R. T. Williams, *et al.*, "Experimental and computational results on exciton/free-carrier ratio, hot/thermalized carrier diffusion, and linear/nonlinear rate constants affecting scintillator proportionality," *Proc. SPIE* 8852 (2013);

[6] J. Q. Grim, *et al.,* "Nonlinear quenching of densely excited states in wide-gap solids," *Phys. Rev. B* **87**, 125117 (2013);

[7] E. Kioupakis, *et al.*, "First-principles calculations of indirect Auger recombination in nitride semiconductors,"

[8] E. Kioupakis, *et al.*, "Indirect Auger recombination as a cause of efficiency droop in nitride light-emitting diodes," *Appl. Phys. Lett.* **98**, 161107 (2011);

[9] G. Bizarri, *et al*., "Progress in Studying Scintillator Proportionality: Phenomenological Model", IEEE Trans. Nucl. Sci. **59**, 2038 (2012);

[10] R. T. Williams, *et al.*, "Experimental and computational results on exciton/free-carrier ratio, hot/ thermalized carrier diffusion, and linear/nonlinear rate constants affecting scintillator proportionality" Proc. SPIE 8852, 88520J (2013).

[11] Q. Li, et al., "Host structure dependence of light yield and proportionality in scintillators in terms of hot and thermalized carrier transport", Phys. Status Solidi RRL **6**(8), 346–348 (2012)

[12] Q. Li, et al., "A transport-based model of material trends in nonproportionality of scintillators", J. Appl. Phys. **109**, 123716 (2011)

[13] K. Yang, et al., "Scintillation kinetics and thermoluminescence of $SrI_2:Eu^{2+}$ single crystals", J. Lumin. **132**, 1824 (2012)

[14] E. V. D. van Loef, *et al.*, "High-energy-resolution scintillator: Ce^{3+} activated $LaBr_3$," *Appl. Phys. Lett.* 79, 1573 (2001);

[15] P. Dorenbos, *et al.*, "Level location and spectroscopy of Ce^{3+}, Pr^{3+}, Er^{3+}, and Eu^{2+} in $LaBr_3$," *J. Lumin.* 117, 147 (2006);

[16] F. P. Doty, et al., "Structure and properties of lanthanide halides," *Proc. SPIE* **6707**, 670705 (2007);

[17] G. Bizarri and P. Dorenbos, "Charge carrier and exciton dynamics in LaBr3:Ce^{3+} scintillators: Experiment and model," *Phys. Rev. B* **75**, 184302 (2007);

[18] D. J. Singh, "Structure and optical properties of high light output halide scintillators," *Phys. Rev. B* **82**, 155145 (2010);

[19] A. Canning, *et al.*, "First-principles study of luminescence in Ce-doped inorganic scintillators," *Phys. Rev. B* **83**, 125115 (2011);

[20] D. Åberg, B. Sadigh, and P. Erhart, "Electronic structure of $LaBr_3$ from quasi-particle self-consistent GW calculations," *Phys. Rev. B* **85**, 125134 (2012).

[21] K. Yang, *et al.*, "Performance improvement of large Sr2+ and Ba2+ co-doped LaBr3:Ce3+ scintillation crystals," IEEE Nuclear Science Symposium and Medical Imaging Conference (NSS/MIC) 308 (2012);

[22] M. S. Alekhin, *et al.,* "Improvement of γ-ray energy resolution of $LaBr_3:Ce^{3+}$ scintillation detectors by Sr^{2+} and Ca^{2+} co-doping," *Appl. Phys. Lett.* 102, 161915;

[23] M. S. Alekhin, *et al.,* "Improvement of $LaBr_3$:5%Ce scintillation properties by Li^+, Na^+, Mg^{2+}, Ca^{2+}, Sr^{2+}, and Ba^{2+} co-doping," *J. Appl. Phys.* **113**, 224904 (2013);

[24] M. S. Alekhin, *et al.,* "Optical properties and defect structure of Sr^{2+} co-doped $LaBr_3$:5%Ce scintillation crystals," *J. Lumin.* **145**, 518 (2014);

[25] D. Åberg, B. Sadigh, A. Schleife, and P. Erhart, "Origin of resolution enhancement by co-doping of scintillators: Insight from electronic structure calculation," *Appl. Phys. Lett.* **104**, 211908 (2014).

[26] P. Erhart, B. Sadigh, A. Schleife, and D. Åberg, "A first-principles study of co-doping in lanthanum bromide," Phys. Rev. B, **91**, 165206 (2015)

[27] J. L. Gavartin, et al., "Modeling charge self-trapping in wide-gap dielectrics: Localization problem in local density functionals," Phys. Rev. B 67, 035108 (2003);

[28] S. Lany and A. Zunger, “Polaronic hole localization and multiple hole binding of acceptors in oxide wide-gap semiconductors,” Phys. Rev. B **80**, 085202 (2009);
[29] Dabo, et al., “Koopmans’ condition for density-functional theory,” Phys. Rev. B **82**, 115121(2010);
[30] P. Erhart, A. Klein, D. Åberg, and B. Sadigh, “Efficacy of the DFT+ U formalism for modeling hole polarons in perovskite oxides,” Phys. Rev. B **90**, 035204 (2014).
[31] S. N. Kerisit , et al., “Kinetic Monte Carlo simulations of scintillation processes in NaI(Tl),” IEEE Trans. Nucl. Sci. **61**, 860-869
[32] R.D. Popp and R. B. Murray, “Diffusion of the V_k-polaron in alkali halides: Experiments in NaI and RbI”, J. Phys. Chem. Solids **33**, 601 (1972)
[33] T. Pawlik and J.-M. Spaeth, “Electron and hole centres in the x-irradiated elpasolite crystal Cs_2NaYCl_6 studied by means of electron paramagnetic resonance and electron nuclear double resonance”, J. Phys.: Condens. Matter **9**, 8737 (1997)
[34] K. Biswas and M.-H. Du, “Energy transport and scintillation of cerium-doped elpasolite Cs_2LiYCl_6: Hybrid density functional calculations”, Phys. Rev. B **86**, 014102 (2012).

6.0 TECHNICAL REPORTS/PUBLICATIONS (BY TASK):

6.1 Publications

1. "*First principles calculations and experiment predictions for iodine vacancy centers in SrI_2*", Qi Li, Richard Williams, and Daniel Åberg, Phys. Stat. Solidi **250**, 233 (2013)

2. "*Quasiparticle spectra, absorption spectra, and excitonic properties of NaI and SrI_2 from many-body perturbation theory*", Paul Erhart, André Schleife, Babak Sadigh, and Daniel Åberg, Phys. Rev. B **89**, 075132 (2014)

3. *"Origin of resolution enhancement by co-doping of scintillators: Insight from electronic structure calculations",* Daniel Åberg, Babak Sadigh, André Schleife, and Paul Erhart, Appl. Phys. Lett, **104**, 211908 (2014)

4. *"Efficacy of the DFT + U formalism for modeling hole polarons in perovskite oxides",* Paul Erhart, Andreas Klein, Daniel Åberg, and Babak Sadigh, Phys. Rev. B **90**, 035204 (2014)

5. "*First principles study of co-doping in lanthanum bromide*", Paul Erhart, Babak Sadigh, and Daniel Åberg, Phys. Rev. B, **91**, 165206 (2015)

6. *"Auger recombinetion in sodium-iodide scintillators from first principles"*, Andrew McAllister, Daniel Aberg, André Schleife, and Emmanouil Kioupakis, Appl. Phys. Lett. **106**, 141901 (2015)

7. *"Variational polaron self-interaction-corrected total-energy functional for charge excitations in insulators"*, Phys. Rev. B **92**, 075202 (2015)

6.2 Presentations

1. "*Polarons and Excitons in Halide Scintillator"*, Invited presentation at the APS 2013 March Meeting in Baltimore, MD.
2. "*A variational polaron-self-interaction corrected total-energy functional for charge excitations in wide-gap insulators*", Oral presentation, APS 2014 March Meeting in Denver, CO.
3. *"An $O(h^2)$ Coulomb singularity correction for the Bethe-Salpeter equation"*, Oral presentation, APS 2014 March Meeting in Denver, CO.
4. "*Polarons in Scintillating Materials"*, Invited presentation at the Workshop for Scintillation Mechanisms in Gamma Detectors, Washington D.C, April 17, 2014
5. *"First Principles Modeling of Mechanisms Underlying Scintillator Non-Proportionality"*, Presented at the Nuclear Weapons & Material Security Team Program Review Meeting (WMS 2014), Argonne National Laboratory, May 22, 2014
6. *"Resolution Enhancement by Co-Doping of $LaBr_3$(Ce): Insight from Electronic Structure Calculations"*, Oral presentation at MRS 2014 Fall Meeting in Boston, MA
7. *"Parameter-Free Calculation of Optical and Energy Loss Spectra of NaI, $LaBr_3$, BaI_2, and SrI_2 Scintillator Materials"*, Oral presentation at MRS 2014 Fall Meeting in Boston, MA
8. *"A first-principles study of co-doping in lanthanum bromide"*, D. Åberg, B. Sadigh, A. Schleife, and P. Erhart, presented at the APS March Meeting 2015, in San Antonio (TX)